Electron scattering and photoionization of one-electron diatomic molecules

Haruhide Miyagi, Toru Morishita,* and Shinichi Watanabe
Department of Engineering Science, University of Electro-Communications, 1-5-1 Chofu-ga-oka, Chofu-shi, Tokyo 182-8585, Japan
(Received 24 November 2011; published 15 February 2012)

We develop an efficient numerical procedure for solving the scattering problem on one-electron diatomic molecules in the fixed-nuclei approximation. For this purpose, we use the R-matrix propagation method together with the discrete variable representation method in prolate spheroidal coordinates. The demonstrated elastic scattering differential cross sections and the photoionization differential cross sections for H_2^+ and HeH^{2+} exhibit oscillating structures owing to the two-center nature of the molecules. We analyze them by using the Coulomb corrected independent-atom model to identify the two-center quantum interference, and it is found that multiple-scattering effects become important in the heteronuclear system.

DOI: 10.1103/PhysRevA.85.022708 PACS number(s): 34.80.Bm, 33.80.−b, 31.15.−p

I. INTRODUCTION

Electron scattering and photoionization (PI) of molecules have been investigated extensively over the past decades, both theoretically and experimentally, and provided numerous useful information for various applied fields such as plasma physics, astrophysics, and radiation physics. Following the recent developments in intense laser technologies, it has also become clear that electron scattering by a molecular ion is fundamental to the understanding of molecular structures and dynamics under strong laser fields. When a molecule is exposed to an intense laser pulse, an electron can be tunnel-ionized, then accelerated until it is driven back by the oscillating electric field of the laser to recollide with the parent ion [1,2]. This re-encounter incurs various elastic and inelastic electron-molecular ion collision phenomena. Indeed, it is shown that elastic scattering (ES) cross sections and PI cross sections can be extracted from the above-threshold ionization spectra and high-order harmonic spectra for various atoms and aligned molecules [3–21]. Moreover, it is demonstrated with rare gas atoms [22] that the effective electron-ion interaction potential can be accurately retrieved from the experimental above-threshold ionization spectra. It is also shown that $(e,2e)$ and electron impact excitation cross sections play an important role in explaining the nonsequential double ionization of He, Ar, and Ne [23–26]. Further understanding of such recollision phenomena as well as retrieval of ultrafast molecular dynamics during the recollision within a laser cycle [27,28] requires detailed studies of electron-molecular ion scattering based on accurate theoretical calculations. In this paper we employ a rigorous method of calculating the scattering states of one-electron diatomic molecules in the fixed-nuclei approximation, taking advantage of the prolate spheroidal coordinates where the Coulomb singularities pose no difficulty. Although the prolate spheroidal coordinates permitted us to solve the scattering problem of one electron with two fixed nuclei analytically [29], implementing accurate numerical calculations for further study waited for a while. A series of papers on accurate numerical methods for spheroidal Coulomb phase shift [30–34] appeared in the 1970s. Having obtained the spheroidal Coulomb phase shift, Della Picca *et al.* [35], Tao *et al.* [36], and Guan *et al.* [37] showed the differential PI cross sections of H_2^+ by using accurate scattering wave functions. Then PI cross sections were used to analyze calculated high-order harmonics spectra of H_2^+ generated by intense laser pulses [38]. Their studies were limited to the ground state of H_2^+. No theoretical calculations in the prolate spheroidal coordinates for PI spectra seem to have been done for heteronuclear molecules such as HeH^{2+} in which the dipole effect becomes important. Note that the role of the permanent dipole in polar molecules in strong-field phenomena has attracted much attention in experiment and theory recently [39–45].

In this paper, we obtain accurate scattering wave functions as well as scattering matrices (S matrices) for arbitrary combinations of nuclear charge states by matching to the asymptotic wave function, which includes the effects of the dipole term in addition to the Coulomb interactions. We demonstrate the ES differential cross sections (DCSs) and the photoionization (PI) DCSs of HeH^{2+} as well as H_2^+. As for the ES DCS, electron scattering by two fixed nuclei is impossible for conventional electron beam experiments, but it becomes a physically realizable problem using laser-induced electron rescattering.

As we shall see later, the angular distributions of the ES DCSs and PI DCSs exhibit oscillating structures owing to the two-center nature of the molecules. We develop the Coulomb corrected independent atom model (CCIAM), where the scattering amplitude is approximated by the sum of the Coulomb scattering amplitude satisfying the asymptotic Coulomb boundary condition, to identify the two-center quantum interference in the two Coulomb potentials in those structures.

This article is organized as follows. The scattering theory for one-electron diatomic molecules in prolate spheroidal coordinates is described in Sec. II. Explicit forms of the scattering wave functions and the S-matrix elements are derived. In Sec. III, the numerical procedure for calculating the scattering problem is described in detail. In Sec. IV, the ES DCSs and PI DCSs of H_2^+ and HeH^{2+} are demonstrated. Section V summarizes this article. Unless otherwise stated, atomic units are used throughout the article.

*toru@pc.uec.ac.jp

II. SCATTERING THEORY IN PROLATE SPHEROIDAL COORDINATES

A. Spheroidal phase shift, S matrix, and scattering wave function

We consider an electron scattered by two nuclei with charge states Z_1 and Z_2, located at $z = -R/2$ and $R/2$, respectively. The Schrödinger equation for the system in the molecular frame reads

$$\left(-\frac{1}{2}\nabla^2 - \frac{Z_1}{r_1} - \frac{Z_2}{r_2}\right)\Psi(\boldsymbol{r}) = E\Psi(\boldsymbol{r}), \tag{1}$$

where r_1 and r_2 are the distances of the electron from the nuclear charges, Z_1 and Z_2, respectively. Using the prolate spheroidal coordinates defined by

$$\begin{aligned} \xi &= (r_1 + r_2)/R (1 \leqslant \xi < \infty), \\ \eta &= (r_1 - r_2)/R (-1 \leqslant \eta < 1), \\ \phi &= \arctan(y/x) \quad (0 \leqslant \phi \leqslant 2\pi), \end{aligned} \tag{2}$$

we rewrite Eq. (1) as follows:

$$\begin{aligned} &\left\{ -\frac{1}{2}\frac{4}{R^2}\left[\frac{1}{\xi^2-\eta^2}\left(\frac{\partial}{\partial\xi}(\xi^2-1)\frac{\partial}{\partial\xi} + \frac{\partial}{\partial\eta}(1-\eta^2)\frac{\partial}{\partial\eta}\right)\right.\right. \\ &\left.\left. + \frac{1}{(\xi^2-1)(1-\eta^2)}\frac{\partial^2}{\partial\phi^2}\right] - \frac{2}{R}\frac{(Z_1+Z_2)\xi + (Z_2-Z_1)\eta}{\xi^2-\eta^2}\right\} \\ &\Psi(\boldsymbol{r}) = E\Psi(\boldsymbol{r}). \end{aligned} \tag{3}$$

By expressing the solution in the form

$$\Psi(\boldsymbol{r}) = \Pi^k_{|m|q}(\xi)\Xi^k_{|m|q}(\eta)\frac{e^{im\phi}}{\sqrt{2\pi}}, \tag{4}$$

Eq. (3) is decomposed into two separable equations in ξ and η,

$$\begin{aligned} &\left[\frac{d}{d\eta}(1-\eta^2)\frac{d}{d\eta} - \frac{m^2}{1-\eta^2} + c^2(1-\eta^2)\right. \\ &\left. + b\eta + \lambda_{mq}\right]\Xi^k_{|m|q}(\eta) = 0, \end{aligned} \tag{5}$$

$$\begin{aligned} &\left[\frac{d}{d\xi}(\xi^2-1)\frac{d}{d\xi} - \frac{m^2}{\xi^2-1} + c^2(\xi^2-1)\right. \\ &\left. + a\xi - \lambda_{mq}\right]\Pi^k_{|m|q}(\xi) = 0, \end{aligned} \tag{6}$$

where $m = 0, \pm 1, \ldots$ is the azimuthal quantum number, $q = 0, 1, \ldots$ represents the number of zeros in η, and λ_{mq} is the separation constant. The new symbols a, b, and c are also introduced [31,34]:

$$a = R(Z_2 + Z_1), \quad b = R(Z_2 - Z_1), \quad c = \frac{\sqrt{2E}R}{2}. \tag{7}$$

For a given value of $|m|$, the spheroidal angular wave function, $\Xi^k_{|m|q}(\eta)$, and the spheroidal radial wave function, $\Pi^k_{|m|q}(\xi)$, with different q are orthogonal and they are normalized by

$$\int_{-1}^{1}\Xi^k_{|m|q}(\eta)\Xi^k_{|m|q'}(\eta)d\eta = \delta_{qq'} \tag{8}$$

and

$$\frac{R^3}{8}\int_1^\infty(\xi^2-1)\Pi^k_{|m|q}(\xi)\Pi^{k'}_{|m|q}(\xi)d\xi = \delta(k-k'), \tag{9}$$

respectively. The regular solution of Eq. (6) with

$$\Pi^k_{|m|q}(\xi) \propto (\xi^2-1)^{|m|/2} \quad (\xi \to 1) \tag{10}$$

has the asymptotic form [31,34,37]

$$\Pi^k_{|m|q}(\xi) \xrightarrow{\xi\to\infty} \frac{N_k}{c\xi}\sin\left(c\xi - \frac{L\pi}{2} - \gamma\ln(2c\xi) + \Delta_{|m|q}\right), \tag{11}$$

where $L = |m| + q$, $\gamma = -(Z_1+Z_2)/k$, $\Delta_{|m|q}$ is the spheroidal phase shift, and $N_k = k\sqrt{2/\pi}$ is determined by the momentum-normalization condition, Eq. (9). If the energy-normalization condition is employed, i.e., $\delta(E-E')$ is used instead of $\delta(k-k')$ in Eq. (9), the factor N_k should be replaced by $N_E = \sqrt{2k/\pi}$.

The S matrix and the scattering wave functions, which are used for the calculations of the ES and PI cross sections, are obtained from $\Delta_{|m|q}$. The asymptotic form of the scattering wave function $\Psi^{(+)}_{\boldsymbol{k}_\mathrm{i}}(\boldsymbol{r})$ with the incident $[\boldsymbol{k}_\mathrm{i} = (k,\theta_\mathrm{i},\phi_\mathrm{i})]$ and scattering $[\boldsymbol{k}(= k\hat{\boldsymbol{r}}) = (k,\theta,\phi)]$ wave vectors, satisfying the outgoing wave boundary condition, is expressed in the partial wave expansion,

$$\begin{aligned} \Psi^{(+)}_{\boldsymbol{k}_\mathrm{i}}(\boldsymbol{r}) \xrightarrow{r\to\infty} &\sum_{m=-\infty}^{\infty}\sum_{l=|m|}^{\infty}\sum_{l'=|m|}^{\infty}\frac{1}{\sqrt{2\pi}}\frac{i^{l+1}}{kr} \\ &\times\left[e^{-i(kr-l\pi/2-\gamma\ln 2kr)} - S^{|m|}_{l'l}e^{i(kr-l\pi/2-\gamma\ln 2kr)}\right] \\ &\times Y^*_{lm}(\hat{\boldsymbol{k}}_\mathrm{i})Y_{l'm}(\hat{\boldsymbol{k}}), \end{aligned} \tag{12}$$

where $S^{|m|}_{l'l}$ represents the S-matrix element for a given value of $|m|$. We also expand $\Psi^{(+)}_{\boldsymbol{k}_\mathrm{i}}(\boldsymbol{r})$ with respect to a complete set of the eigenfunctions in Eq. (4):

$$\Psi^{(+)}_{\boldsymbol{k}_\mathrm{i}}(\boldsymbol{r}) = \sum_{m=-\infty}^{\infty}\sum_{q=0}^{\infty}b_{mq}\Pi^k_{|m|q}(\xi)\Xi^k_{|m|q}(\eta)\frac{e^{im\phi}}{\sqrt{2\pi}}. \tag{13}$$

By comparing Eq. (12) with the asymptotic form of Eq. (13), using Eq. (11), we find

$$b_{mq} = \frac{1}{k}e^{i\Delta_{|m|q}}i^{-L}\Xi^k_{|m|q}(-\cos\theta_\mathrm{i})\frac{e^{-im(\phi_\mathrm{i}+\pi)}}{\sqrt{2\pi}} \tag{14}$$

and

$$S^{|m|}_{l'l} = i^{l+l'}\sum_{q=0}^{\infty}A^{|m|}_{ql}\exp[i(2\Delta_{|m|q} - \pi L)]A^{|m|}_{ql'}, \tag{15}$$

where

$$A^{|m|}_{ql} = \sqrt{\frac{2l+1}{2}\frac{(l-|m|)!}{(l+|m|)!}}\int_{-1}^{1}\Xi^k_{|m|q}(\eta)P^{|m|}_l(\eta)d\eta \tag{16}$$

is the unitary transformation matrix between the angular functions in the spherical and spheroidal coordinates.

B. Scattering amplitude and elastic scattering cross section

After getting the S matrix in Eq. (15) in the previous subsection, we turn to the formulation of elastic electron scattering. The ES DCS in the molecular frame is given by $d\sigma/d\Omega = |f(\boldsymbol{k},\boldsymbol{k}_\mathrm{i})|^2$, where the scattering amplitude, $f(\boldsymbol{k},\boldsymbol{k}_\mathrm{i})$,

is defined by the following asymptotic form of the scattering wave function:

$$\Psi^{(+)}_{\boldsymbol{k}_\mathrm{i}}(\boldsymbol{r}) \xrightarrow{r\to\infty} \frac{1}{(2\pi)^{3/2}}\left(e^{i\boldsymbol{k}_\mathrm{i}\cdot\boldsymbol{r}+i\gamma\ln[kr(1-\hat{\boldsymbol{k}}_\mathrm{i}\cdot\hat{\boldsymbol{r}})]} + f(\boldsymbol{k},\boldsymbol{k}_\mathrm{i})\frac{e^{ikr-i\gamma\ln 2kr}}{r}\right). \quad (17)$$

It is well known that the convergence of the partial wave expansion of the scattering amplitude for Coulomb systems is extremely slow. Thus we decompose the scattering amplitude into the long-range (f^c) and short range (f') parts,

$$f(\boldsymbol{k},\boldsymbol{k}_\mathrm{i}) = f^c(\boldsymbol{k},\boldsymbol{k}_\mathrm{i}) + f'(\boldsymbol{k},\boldsymbol{k}_\mathrm{i}), \quad (18)$$

expressing the long-range part in the analytic form [46]

$$f^c(\boldsymbol{k},\boldsymbol{k}_\mathrm{i}) = -\frac{\gamma e^{-i\gamma\ln(\sin^2\frac{\theta_k}{2})+2i\sigma_0}}{2k\sin^2\frac{\theta_k}{2}}e^{i\boldsymbol{r}_{\mathrm{CC}}\cdot(\boldsymbol{k}-\boldsymbol{k}_\mathrm{i})}, \quad (19)$$

where $\theta_k = \cos^{-1}(\hat{\boldsymbol{k}}\cdot\hat{\boldsymbol{k}}_\mathrm{i})$, and $\sigma_l = \arg\Gamma(l+1+i\gamma)$. $f^c(\boldsymbol{k},\boldsymbol{k}_\mathrm{i})$ is equivalent to the Coulomb scattering amplitude for Z_1+Z_2 centered about $\boldsymbol{r}_{\mathrm{CC}}$. We choose the center to be the center of nuclear charges in order to incorporate the dipole as well as the Coulomb interactions in the asymptotic region in the molecular potential, i.e.,

$$\boldsymbol{r}_{\mathrm{CC}} = \left(0,0,\frac{R(Z_2-Z_1)}{2(Z_1+Z_2)}\right)^t. \quad (20)$$

The short-range part $f'(\boldsymbol{k},\boldsymbol{k}_\mathrm{i})$ associated with the remainder of the potential, $-Z_1/r_1 - Z_2/r_2 + (Z_1+Z_2)/|\boldsymbol{r}-\boldsymbol{r}_{\mathrm{CC}}|$, is evaluated by the partial-wave expansion,

$$f'(\boldsymbol{k},\boldsymbol{k}_\mathrm{i}) = \sum_{m=-\infty}^{\infty}\sum_{l=|m|}^{\infty}\sum_{l'=|m|}^{\infty}\frac{2\pi i}{k}i^{l-l'} \times\left(\tilde{S}^{|m|}_{l'l} - S^{|m|}_{l'l}\right)Y^*_{lm}(\hat{\boldsymbol{k}}_\mathrm{i})Y_{l'm}(\hat{\boldsymbol{k}}), \quad (21)$$

where

$$\tilde{S}^{|m|}_{l'l} = \sum_{l''=|m|}^{\infty}B^{|m|}_{l'l''}e^{2i\sigma_{l''}}B^{|m|*}_{l''l}, \quad (22)$$

$$B^{|m|}_{l'l''} = \int Y^*_{l'|m|}(\hat{\boldsymbol{k}})e^{i\boldsymbol{k}\cdot\boldsymbol{r}_{\mathrm{CC}}}Y_{l''|m|}(\hat{\boldsymbol{k}})d\hat{\boldsymbol{k}}. \quad (23)$$

The partial-wave expansion in Eq. (21) is converged rapidly and thus the cross sections can be calculated efficiently for heteronuclear as well as homonuclear molecules. We find that the inclusion of $|m| = 0,\ldots,80$ and $l = |m|,\ldots,|m|+80$ for a given value of m is sufficient to obtain converged ES DCSs for the incident energy of $\leqslant$150 eV as shown in Sec. IV A.

The ES DCS in the laboratory frame $d\sigma/d\Omega'$ is obtained by the frame transformation of the spherical harmonics in the scattering amplitudes in Eq. (21),

$$Y_{l'm}(\hat{\boldsymbol{k}}) = \sum_{m'=-l'}^{l'}\mathscr{D}^{l'}_{m'm}(0,\Theta,0)Y_{l'm'}(\hat{\boldsymbol{k}}'), \quad (24)$$

where $\mathscr{D}^{l'}_{m'm}(0,\Theta,0)$ is the Wigner function, with Θ being the angle between the molecular and the laboratory frame axes. In this article, primed (unprimed) symbols pertain to the laboratory (molecular) frame.

C. Dipole transition amplitude and photoionization cross section

We move on to the formulation of the PI cross section. Within the framework of the perturbation theory, the PI DCS with photoelectron momentum $\boldsymbol{k} = (k,\theta_k,\phi_k)$ in the molecular frame in the dipole length form reads

$$\frac{d\sigma_{\mathrm{ph}}}{d\Omega} = 4\pi^2\omega k\alpha|\langle\Psi^{(-)}_{\boldsymbol{k}}|\hat{\boldsymbol{\epsilon}}\cdot\boldsymbol{r}|\Psi_\mathrm{g}\rangle|^2, \quad (25)$$

where α is the fine-structure constant, $\hat{\boldsymbol{\epsilon}} = \sin\Theta_\varepsilon\hat{\boldsymbol{x}} + \cos\Theta_\varepsilon\hat{\boldsymbol{z}}$ is the polarization direction, and ω is the angular frequency of the incident radiation. Θ_ε indicates the polarization angle in the molecular frame. The initial ground-state wave function Ψ_g is obtained by diagonalizing the Hamiltonian using the direct product of the discrete variable representation (DVR) basis sets associated with Legendre polynomials [47,48]. (See Appendix C.) The final-state wave function satisfying the incoming-wave boundary condition, $\Psi^{(-)}_{\boldsymbol{k}}(\boldsymbol{r}) = [\Psi^{(+)}_{-\boldsymbol{k}}(\boldsymbol{r})]^*$, is constructed from Eqs. (13) and (14) together with the numerical procedure described in the next section. Since we consider the PI of the ground states with the σ symmetry, the dipole transition amplitude in Eq. (25) can be simplified in the form

$$\langle\Psi^{(-)}_{\boldsymbol{k}}|\hat{\boldsymbol{\epsilon}}\cdot\boldsymbol{r}|\Psi_\mathrm{g}\rangle = m_\sigma\cos\Theta_\varepsilon + m_\pi\sin\Theta_\varepsilon, \quad (26)$$

where

$$m_\sigma = \sum_{q=0}^{\infty}\Xi^k_{0q}(\cos\theta_k)\frac{1}{\sqrt{2\pi}}\frac{R^3}{8}\int\psi_{0q}(\xi,\eta)r\cos\theta\Psi_\mathrm{g} \times(\xi,\eta)(\xi^2-\eta^2)d\xi d\eta, \quad (27)$$

$$m_\pi = \sum_{q=0}^{\infty}\Xi^k_{1q}(\cos\theta_k)\sqrt{\frac{2}{\pi}}\cos\phi_k\frac{R^3}{8}\int\psi_{1q}(\xi,\eta)r\sin\theta\Psi_\mathrm{g} \times(\xi,\eta)(\xi^2-\eta^2)d\xi d\eta, \quad (28)$$

and

$$r\cos\theta = \frac{R}{2}\xi\eta, \quad (29)$$

$$r\sin\theta = \frac{R}{2}\sqrt{(\xi^2-1)(1-\eta^2)}, \quad (30)$$

$$\psi_{|m|q}(\xi,\eta) = \frac{1}{k}e^{i\Delta_{|m|q}}i^{-L}\Pi^k_{|m|q}(\xi)\Xi^k_{|m|q}(\eta). \quad (31)$$

The integrations in Eqs. (27) and (28) are carried out with the Gauss-Legendre quadrature points. We find that the inclusion of $q = 0,\ldots,25$ in the summations in Eqs. (27) and (28) is sufficient to obtain converged angular distributions of PI cross sections, which is much fewer than is the case for electron scattering. We also have implemented PI DCS calculations using the diopole velocity and accelaration forms in addition to the length form in Eq. (25) and comfirmed perfect agreements among the three forms.

The PI DCS in the laboratory frame $d\sigma_{\mathrm{ph}}/d\Omega'$ is obtained by the frame transformation of the angular functions in Eqs. (27)

and (28):

$$\Xi^k_{|m|q}(\cos\theta_k)\frac{e^{im\phi_k}}{\sqrt{2\pi}} = \sum_{l=|m|}^{\infty} A^{|m|}_{ql}(k,R) i^{m+|m|} \times \sum_{m'=-l}^{l} \mathscr{D}^l_{m'm}(0,\Theta,0) Y_{lm'}(\hat{\boldsymbol{k}}'). \quad (32)$$

III. NUMERICAL PROCEDURE

A. Spheroidal angular part

Solving the spheroidal angular equation, (5), we have to pay attention to the fact that the spheroidal angular functions for odd m are not analytic at the boundaries of $\eta = \pm 1$, satisfying the condition

$$\Xi^k_{|m|q}(\eta) \propto (1-\eta^2)^{|m|/2} \quad (\eta \to \pm 1). \quad (33)$$

In Ref. [36], different numerical procedures based on the DVR method are used for even and odd m. In this paper, we develop another numerical implementation for both even and odd m on equal footing by introducing a new variable, y:

$$\sqrt{1-\eta^2} = 1 - y^2 \quad (-1 \leqslant y \leqslant 1). \quad (34)$$

Then we rewrite Eq. (5) in the form

$$(K + V - \lambda_{mq} S)\Xi^k_{|m|q}[\eta(y)] = 0, \quad (35)$$

with

$$K = -\frac{d}{dy}\frac{1}{2}(1-y^2)(2-y^2)^{1/2}\frac{d}{dy}, \quad (36)$$

$$V = \frac{2m^2}{(1-y^2)(2-y^2)^{1/2}} - \frac{2(1-y^2)}{(2-y^2)^{1/2}} \times \left[by(2-y^2)^{1/2} + c^2(1-y^2)^2\right], \quad (37)$$

$$S = \frac{2(1-y^2)}{(2-y^2)^{1/2}}. \quad (38)$$

The solutions to Eq. (35) in variable y are analytic for both even and odd m. Thus we can solve the eigenvalue problem accurately using the DVR basis set associated with Legendre polynomials, $\pi_i(y)$:

$$\Xi^k_{|m|q}[\eta(y)] = \sum_{i=1}^{N_y} c_i \pi_i(y). \quad (39)$$

Substituting Eq. (39) into Eq. (35) and integrating over y by using the quadrature rule [48], we have the eigenvalue problem in the matrix form,

$$[\boldsymbol{S}^{-1/2}(\boldsymbol{K}+\boldsymbol{V})\boldsymbol{S}^{-1/2} - \lambda]\boldsymbol{S}^{1/2}\boldsymbol{c} = \boldsymbol{0}. \quad (40)$$

Since $\boldsymbol{V}$ and $\boldsymbol{S}$ are diagonal in DVR, λ_{mq} and $\{c_i\}_{i=1}^{N_y}$ are easily obtained by numerical diagonalization for a given m. In the present study, the number of DVR quadrature points is typically set to $N_y = 270$.

B. Spheroidal radial part

Substituting λ_{mq} into the spheroidal radial equation, (6), we solve the equation with the R-matrix propagation method and obtain the spheroidal phase shifts $\Delta_{|m|q}$ by matching to the asymptotic boundary condition at a sufficiently large $\xi = \xi_{\rm M} \gg 1$. To begin with, we divide the interval of ξ into $N_{\rm sec}$ sectors:

$$1 = \bar{\xi}_0 < \bar{\xi}_1 < \cdots < \bar{\xi}_{N_{\rm sec}} = \xi_{\rm M}. \quad (41)$$

We treat the first sector and the further sectors in different manners.

First, for the $n(\geqslant 2)$th sector $\bar{\xi}_- \equiv \bar{\xi}_{n-1} \leqslant \xi \leqslant \bar{\xi}_n \equiv \bar{\xi}_+$, we consider the eigenvalue problem

$$\left[\frac{d}{d\xi}(\xi^2-1)\frac{d}{d\xi} - \mathcal{L} - \frac{m^2}{\xi^2-1} + \frac{\bar{E}R^2}{2}(\xi^2-1) + a\xi - \lambda_{mq}\right]\bar{\Pi}_{|m|q}(\xi) = 0, \quad (42)$$

where the Bloch operator,

$$\mathcal{L} = (\xi^2-1)[\delta(\xi-\bar{\xi}_+) - \delta(\xi-\bar{\xi}_-)]\frac{d}{d\xi}, \quad (43)$$

is introduced to Hermitize the equation within the sector. The solutions of Eq. (42) are expanded by the DVR basis set associated with the Legendre polynomials, $\pi_i(x)$ $(i = 1,\ldots,N_x)$:

$$\bar{\Pi}_{|m|q}[\xi(x)] = \sum_{i=1}^{N_x} d_i \pi_i(x). \quad (44)$$

Here, a new variable x $(-1 \leqslant x \leqslant 1)$, defined by

$$\xi(x) = \frac{\bar{\xi}_+ - \bar{\xi}_-}{2}(x+1) + \bar{\xi}_-, \quad (45)$$

is used. We solve the eigenvalue problem, Eq. (42), by numerical diagonalization in the same way as for the spheroidal angular equation in the Sec. III A.

Next, for the first sector, $1 = \bar{\xi}_0 \leqslant \xi \leqslant \bar{\xi}_1$, we use a similar numerical technique to resolve the slow convergence due to the nonanalytic behavior of the radial function for odd m, satisfying the regular boundary condition, Eq. (10). We introduce a new variable,

$$\sqrt{\xi - 1} = \mu, \quad (46)$$

and rewrite Eq. (42) in the form

$$\left[\frac{d}{d\mu}(\mu^3+2\mu)\frac{d}{d\mu} - \frac{4m^2}{\mu^3+2\mu} - \tilde{\mathcal{L}} + 4a(\mu^3+\mu) - 4\mu\lambda_{mq} + 2R^2(\mu^5+2\mu^3)\tilde{E}\right]\tilde{\Pi}_{|m|q}[\xi(\mu)] = 0, \quad (47)$$

where

$$\tilde{\mathcal{L}} = (\mu^3+2\mu)\delta(\mu-\bar{\mu}_+)\frac{d}{d\mu} \quad (48)$$

is the Bloch operator for variable μ, and $\bar{\mu}_+ = \sqrt{\bar{\xi}_1 - 1}$. The solutions to Eq. (47) for both even and odd m are analytic and can be solved easily with the same DVR method as in other sectors by using the scaling

$$\mu(x) = \frac{\bar{\mu}_+}{2}(x+1). \quad (49)$$

Using the spheroidal radial wave functions, the R matrix, defined by

$$\Pi^k_{|m|q}(\xi) = \mathscr{R}_{|m|q}(\xi)\frac{d}{d\xi}\Pi^k_{|m|q}(\xi), \tag{50}$$

is propagated from $\xi = 1$ to $\xi_{\rm M}$ with the boundary condition

$$\mathscr{R}_{|m|q}(\bar{\xi}_0 = 1) = 0. \tag{51}$$

We note that the R matrix is diagonal with respect to the index (m,q). The R matrix at $\xi = \bar{\xi}_1$ is given by the spectral expansion in the first sector using the solution of Eq. (47):

$$\mathscr{R}_{|m|q}(\bar{\xi}_1) = 2\bar{\mu}_+(\bar{\mu}_+^3 + 2\bar{\mu}_+)\sum_{n=1}^{N_x}\frac{(\tilde{\Pi}_{|m|q}[\xi(\bar{\mu}_+)])^2}{\tilde{E}_n - E}. \tag{52}$$

The R-matrix propagation through the further sectors is carried out by using the recurrence relation

$$\mathscr{R}_{|m|q}(\bar{\xi}_+) = \mathcal{R}^{++}_{|m|q} - \frac{(\mathcal{R}^{+-}_{|m|q})^2}{\mathscr{R}_{|m|q}(\bar{\xi}_-) + \mathcal{R}^{--}_{|m|q}}, \tag{53}$$

where

$$\mathcal{R}^{\pm\pm}_{|m|q} = [(\bar{\xi}_\pm^2 - 1)(\bar{\xi}_\pm^2 - 1)]^{1/2}\sum_{n=1}^{N_x}\frac{\bar{\Pi}_{|m|q}(\bar{\xi}_\pm)\bar{\Pi}_{|m|q}(\bar{\xi}_\pm)}{\bar{E}_n - E}. \tag{54}$$

In the asymptotic region of $\xi \geqslant \xi_{\rm M}$, the solution to Eq. (6) can be expressed by the asymptotic expansion,

$$\Pi^{{\rm as},k}_{|m|q}(\xi) \simeq \frac{N_k}{c\xi}\sin\left(c\xi - \frac{L\pi}{2} - \gamma\ln(2c\xi) + \Delta_{|m|q}\right) \times \left(\frac{\xi-1}{\xi+1}\right)^{\frac{m}{2}}\sum_{n=0}^{N} b_n\left(\frac{c\xi}{2}\right)^{-n}, \tag{55}$$

where the values of $\{b_n\}$ are derived in Ref. [33]. The spheroidal phase shift, $\Delta_{|m|q}$, is determined by imposing the matching condition at $\xi_{\rm M}$,

$$\frac{1}{\mathscr{R}_{|m|q}(\xi_{\rm M})} = \frac{1}{\Pi^{{\rm as},k}_{|m|q}(\xi_{\rm M})}\frac{d}{d\xi}\Pi^{{\rm as},k}_{|m|q}(\xi)\Big|_{\xi_{\rm M}}. \tag{56}$$

In the actual calculations, the matching point is estimated by $\xi_{\rm M} \simeq 1500/c$, which ensures the rapid convergence of the asymptotic expansion in Eq. (55) with $N \sim 10$. The number of DVR points $N_x = 10$ is used for all the sectors. The sector size of the first sector is fixed to 0.25. For the further sectors, we choose the sector size to have about 10 sectors per one cycle of the oscillation in the wave function. We comment that several other accurate numerical methods have been used to solve the spheroidal radial equation, such as the Numerov mothod [31] and direct diagonalization with a L^2 basis set [49,50], etc., and the R-matrix method is advantageous to applying to coupled-channel problems for other diatomic molecules in the single-active-electron model, combined with the slow/smooth variable discretization method [51] for further studies.

IV. RESULTS AND DISCUSSION

Our computer code exploits the prolate spheroidal coordinates to solve the scattering problem of one-electron diatomic molecules for a pair of arbitrary nuclear charges at any given nuclear distances. The S matrix and the scattering wave functions, which are now available by implementing the code, are supposed to possess intriguing characteristics due to the two-center nature of the systems. In the following, we illustrate how these are revealed in the ES and PI cross sections. We consider the ES DCSs and PI DCSs of aligned molecules which would be useful for further studies of dynamics of an aligned molecule under an intense laser field.

A. Elastic scattering differential cross sections

1. ES DCSs of H_2^+

Figure 1 presents the ES DCS for H_2^+ at three orientation angles, $\Theta = 0^\circ$, 45°, and 90°, in the laboratory frame, where the incident direction is parallel to the z' axis. Note that the cross section for the orientation angle $180^\circ - \Theta$ is equivalent to that for Θ with ϕ'_k replaced by $180^\circ + \phi'_k$ [see Eq. (24) for the definitions of the primed symbols]. It is therefore sufficient to consider $\Theta \leqslant 90^\circ$. The internuclear distance is set to the equilibrium distance $R = 2$ of the electronic ground state $(1s\sigma_g)$. It is clearly seen from the results for $\Theta = 0^\circ$ that since the long-range Coulomb potential dominates the scattering, as θ'_k decreases, the ES DCS increases monotonically and approaches the one-center Rutherford scattering cross section $(Z_1 + Z_2)^2/[4k^4\sin^4(\theta'_k/2)]$. On the contrary, an oscillating structure appears in the backward scattering where the short-range potential becomes important. For collisions between an electron and a neutral molecule, such a structure is often explained by the two-center quantum interference using the so-called independent atom model (IAM) [52,53]. In the IAM, the net scattering amplitude is approximated by the sum of the contributions from the independent atoms in the molecule. For electron-molecular ion collisions, the Coulomb interaction in the asymptotic region is important. In the present work, we introduce the CCIAM satisfying the correct asymptotic boundary condition at $r \to \infty$. In the CCIAM the scattering amplitude is approximated by the sum of Coulomb amplitudes with effective charges centered at each nucleus, and the cross section is expressed by [see Eqs. (A11), (A12), and (A13) in Appendix A]

$$|f^c(\boldsymbol{k},\boldsymbol{k}_{\rm i})|^2\left\{\frac{Z_1^2 + Z_2^2 + 2Z_1Z_2\cos[\boldsymbol{R}\cdot(\boldsymbol{k}-\boldsymbol{k}_{\rm i})]}{(Z_1+Z_2)^2}\right\}. \tag{57}$$

The overall amplitude of $|f^c(\boldsymbol{k},\boldsymbol{k}_{\rm i})|^2$ is responsible for the Coulomb scattering by the total nuclear charge, and the two-center nature is characterized by the cosine function in the curly brackets representing interference. We note that ES DCS with the CCAIM is invariant with respect to the choice of the origin.

We compare the "exact" calculations with the CCIAM in Fig. 1. We plot the ES DCS for $\Theta = 0^\circ$, and the nodal lines predicted by the interference terms in Eq. (57), i.e.,

$$\boldsymbol{R}\cdot(\boldsymbol{k}-\boldsymbol{k}_{\rm i}) = (2n+1)\pi \quad (n = 0, \pm 1, \dots) \tag{58}$$

for $\Theta = 45^\circ$ and 90°. For the high-energy collision at 150 eV, the CCIAM reproduces the exact results well, including the positions of the two nodal lines in the cross sections. At lower energies, however, discrepancies are larger,

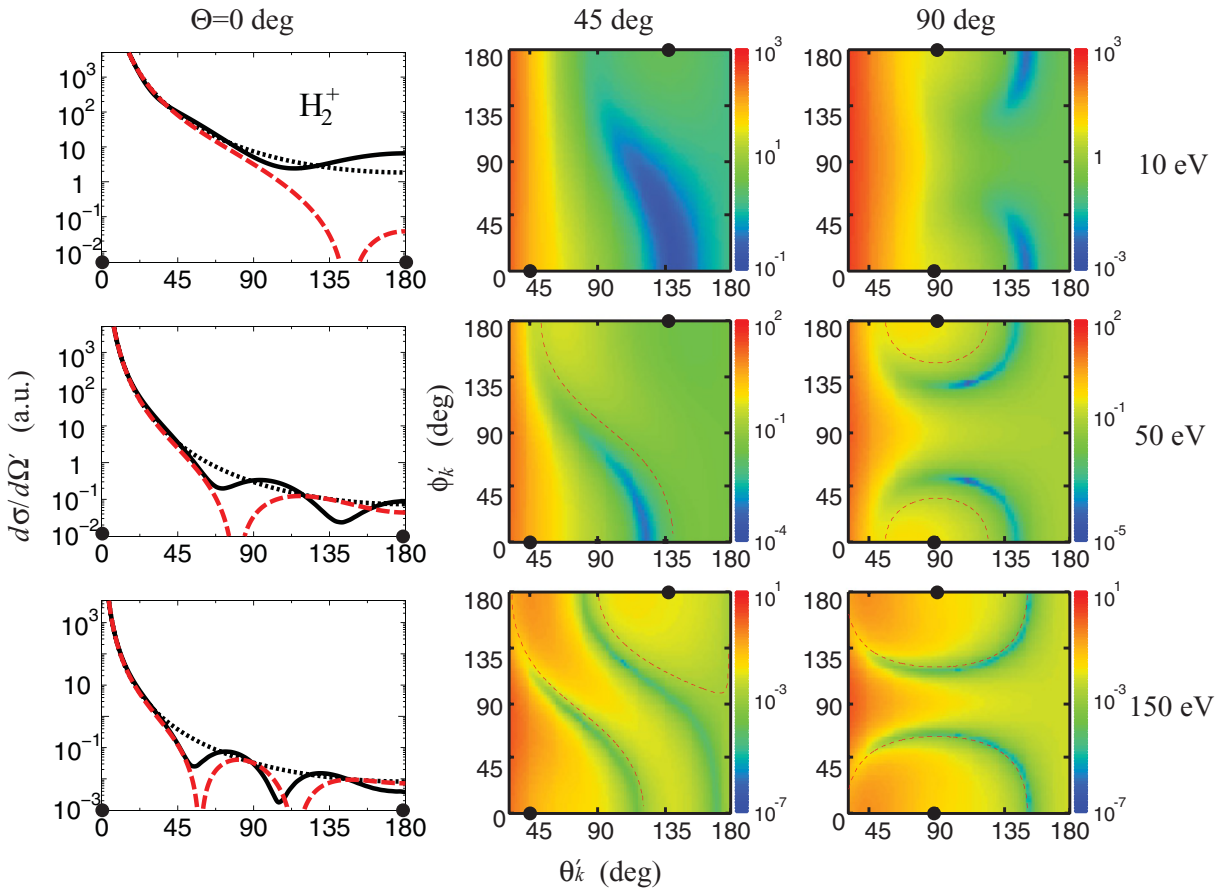

FIG. 1. (Color online) The laboratory frame ES DCSs for fixed-in-space H_2^+ ($R = 2$) for $\Theta = 0°$, 45°, and 90° and for electron energies 10, 50, and 150 eV. The ESCDSs are shown in the $\theta_k'\phi_k'$ plane except for the first column for $\Theta = 0°$, where the ES DCS is independent of the angle ϕ_k'. In the first column, solid (black) curves, accurate ES DCSs; dotted (black) curves, results of one-center Coulomb scattering by total nuclear charge $Z_1 + Z_2$, $|f^c(\boldsymbol{k},\boldsymbol{k}_i)|^2$; and dashed (red) curves, results of the CCIAM [Eq. (57)]. Dashed (red) lines in the two-dimensional ES DCSs indicate the positions of the local minima (nodal lines) predicted by the CCIAM [Eq. (58)]. Filled circles in each panel indicate the directions of the protons.

indicating that a multiple scattering corresponding to the higher order terms in the expansion based on the CCIAM [see Eq. (A9) in Appendix A] becomes important. Indeed, the CCIAM result differs from the exact one by several orders of magnitude in backward scattering for 10 eV at $\Theta = 0°$. Looking in more detail, we find that the CCIAM fails to account for the oscillating structures for 10 eV at $\Theta = 45°$ and 90°, since Eq. (58) has no root.

2. *ES DCSs of HeH²⁺*

Since heteronuclear molecules have no symmetry with respect to $\Theta \leftrightarrow 180° - \Theta$, we have to consider the ES DCSs for the full range of Θ. Here for HeH^{2+}, we plot the cross section at $\Theta = 0°$, 45°, 90°, 135°, and 180° in Fig. 2. We set $R = 2$ to discuss this cross section in parallel with the H_2^+ case. We also plot the ES DCSs with the CCIAM for $\Theta = 0°$ and 180° and the minimum positions from Eq. (58) for the other orientation angles. For smaller orientation angles of $\Theta < 90°$, where the incident electron collides from the He^{2+} side of the molecule, the shapes of the observed ES DCSs are similar to those of H_2^+: The CCIAM results are in good agreement with the exact ones at the higher collision energy of 150 eV, and the CCIAM becomes poor at lower energies. On the contrary, for larger orientation angles of $\Theta > 90°$, where the incident electron collides from the H^+ side of the molecule, large discrepancies can be observed even at 150 eV. For $\Theta = 180°$ the minima in the CCIAM appear at the maxima in the exact cross section. This discrepancy in the positions of the minima is seen even at higher energies (>150 eV). We conclude from these observations that the CCIAM fails to account for the nodal structure for heteronuclear cases. We suspect that the multiple scattering effect plays a very important role in a heteronuclear case such as HeH^{2+}.

B. Photoionization differential cross sections

1. *PI DCSs of H_2^+*

We turn our attention now to examining PI cross sections. The laboratory frame is chosen such that the z' axis is parallel to the polarization vector $\hat{\boldsymbol{\epsilon}}$. In other words, the orientation angle is made opposite to the polarization angle, $\Theta = -\Theta_\varepsilon$. In Fig. 3 we show the PI DCSs of H_2^+ at orientation angles of $\Theta = 0°$, 45°, and 90°. The PI DCS has the same symmetry with respect to Θ and ϕ_k' as does the ES DCS. Namely, the cross section is

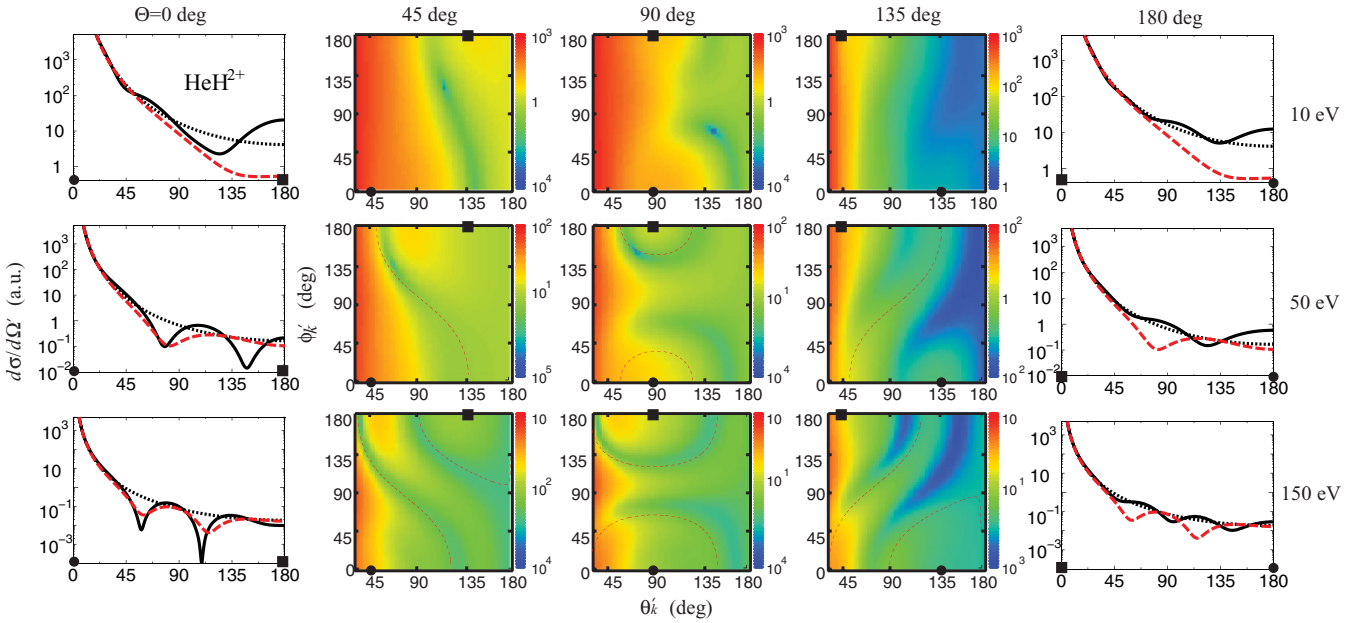

FIG. 2. (Color online) The same as Fig. 1 except ES DCSs for fixed-in-space HeH^{2+} ($Z_1 = 2$, $Z_2 = 1$, and $R = 2$) are shown, and the results for $\Theta = 135^\circ$ and 180° are added. The filled square in each panel indicates the direction of the charge $Z_1 = 2$ (He^{2+}).

invariant under the transformation of $\Theta \leftrightarrow 180^\circ - \Theta$ with ϕ'_k replaced by $180^\circ + \phi'_k$.

We also compare the exact results with the CCIAM. For PI processes, the PI DCS is approximated by replacing $\Psi^{(-)}_{\boldsymbol{k}}(\boldsymbol{r})$ in Eq. (25) with the CCIAM wave function,

$$\frac{Z_1}{Z_1+Z_2}\psi^{(-)}_{\boldsymbol{k},1}(\boldsymbol{r}) + \frac{Z_2}{Z_1+Z_2}\psi^{(-)}_{\boldsymbol{k},2}(\boldsymbol{r}), \tag{59}$$

where $\psi^{(-)}_{\boldsymbol{k},1}(\boldsymbol{r})$ and $\psi^{(-)}_{\boldsymbol{k},2}(\boldsymbol{r})$ are the scattering wave functions by the total nuclear charge of $Z_1 + Z_2$ located at $z = -R/2$ and $R/2$ on the z axis, respectively (see Appendix A). The resulting cross sections are compared with the exact calculations for $\Theta = 0^\circ$ where the molecular axis is parallel to the polarization direction in Fig. 3. For the high photoelectron energy of 150 eV, the CCIAM reproduces the overall shape of the PI DCS including the large peaks at $\theta'_k = 0^\circ$ and 180° as well as the positions of the three local minima, although the absolute value is much larger, by a factor of 10. The agreement becomes worse for lower energies. For 10 eV, the outer peaks at $\theta'_k = 0^\circ$ and 180° are smaller than the inner peaks at 60° and 120° in the CCIAM, while the outer peaks still dominate the inner ones in the exact results. We also found that the CCIAM reproduces the PI DCS for higher energies, >150 eV, at other orientation angles, implying that the two-center nature is explained by the CCIAM in PI as well as in the electron collision.

2. PI DCSs of HeH^{2+}

The PI DCSs of HeH^{2+} for $\Theta = 0^\circ$, 45° and 90° are shown in Fig. 4. The internuclear distance of $R = 2$ is used. The PI DCSs exhibit a remarkable asymmetry due to the heteronuclear nature. Interestingly, we find that the photoelectron tends to be ejected more toward the H^+ side than toward the He^{2+} side. The positions of large peaks at $\theta'_k = 0^\circ$ for $\Theta = 0^\circ$ and at $(\theta'_k, \phi'_k) = (60^\circ, 0^\circ)$ for $\Theta = 45^\circ$ correspond to the direction of H^+. For $\Theta = 90^\circ$, although the photoelectron is not allowed to ionize parallel to the molecular axis, more ionization can be seen at $\phi'_k < 90^\circ$, implying that the photoelectron tends to be ejected toward the H^+ side. This trend can be described by the CCIAM as shown in Fig. 4 for $\Theta = 0^\circ$, while the oscillation appears in out of phase. We found that this is also true for other orientation angles. It is worth noting that the plane-wave approximation to the final states does not explain the asymmetry in the dipole transition amplitude in Eq. (25) of the heteronuclear system at all. Clearly it provides the PI DCSs possessing the symmetry with respect to the transformation of $(\theta'_k, \phi'_k) \leftrightarrow (180^\circ - \theta'_k, 180^\circ + \phi'_k)$. Thus the asymmetry in the final states is very important for heteronuclear systems. We comment that the PI DCS in the CCIAM depends on the choice of the origin. We have checked that the result with the CCIAM in the center of mass of the two nuclei is almost the same as in Fig. 4 in their shapes.

V. SUMMARY

In this paper we have developed an efficient numerical method using prolate spheroidal coordinates for the scattering problem on one-electron diatomic molecules in the fixed-nuclei approximation. The method is based on the R-matrix propagation method together with the DVR method. We have demonstrated a set of accurate results of ES DCSs and PI DCSs for H_2^+ and HeH^{2+}.

Comparing the exact and the CCIAM results, the oscillating structures in the ES DCSs and in PI DCSs have been studied. For H_2^+, structures at electron energies higher than 50 eV are explained as a two-center interference. For HeH^{2+}, however, the CCIAM fails to reproduce the phase of the oscillation in cross sections even at electron energies as high as 150 eV. Thus we conclude that multiple-scattering effects are important in the heteronuclear system.

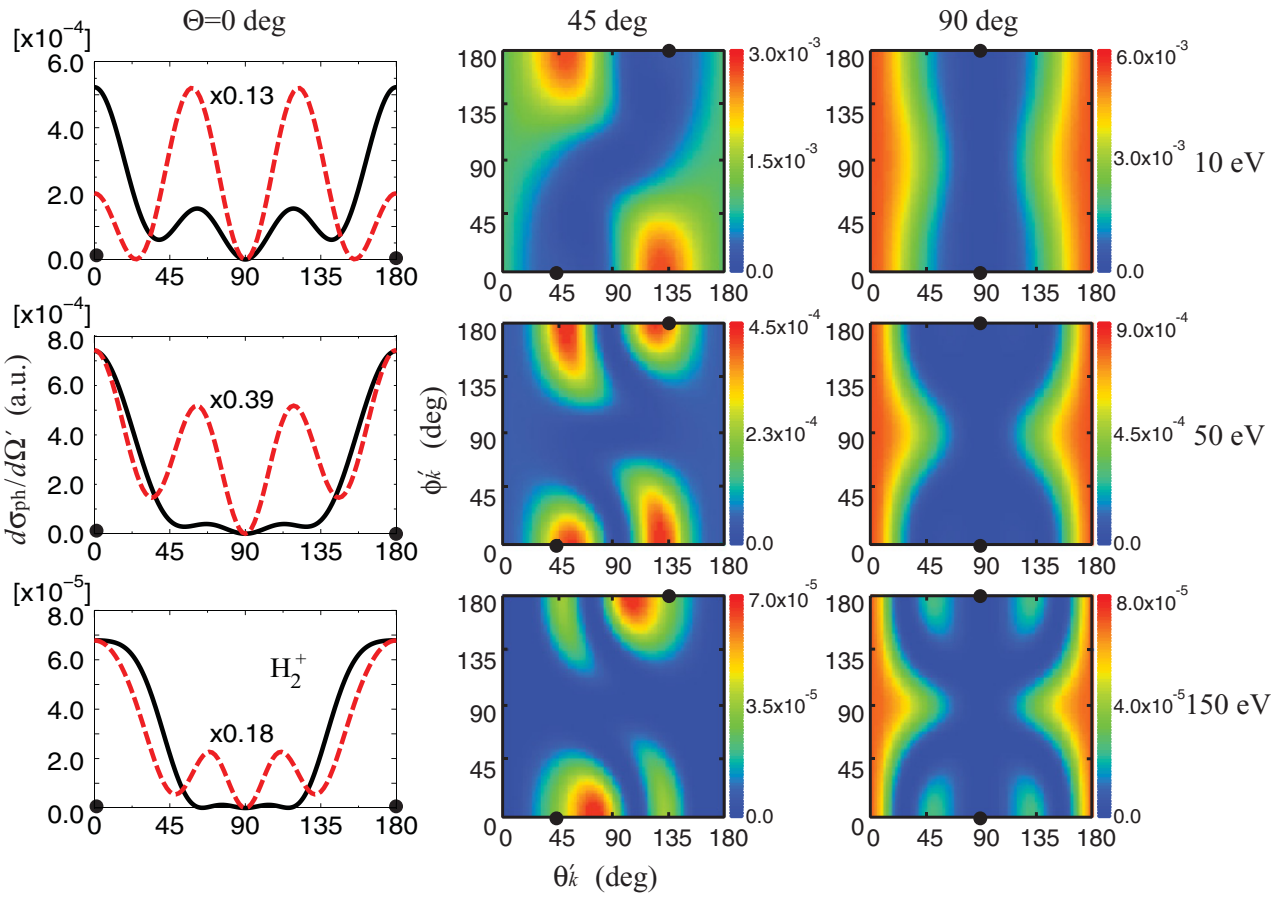

FIG. 3. (Color online) Laboratory-frame PI DCSs for fixed-in-space H_2^+ ($R = 2$) for $\Theta = 0°$, 45°, and 90° and for photoelectron energies 10, 50, and 150 eV. PI DCSs are shown in the $\theta_k'\phi_k'$ plane except in the first column for $\Theta = 0°$, where PI DCSs are independent of the angle ϕ_k'. In the first column, solid (black) curves, accurate PI DCSs; and dashed (red) curves, PI DCSs approximated by the CCIAM. In each panel, two curves are normalized at their maximum value by scaling the dashed (red) curve. Filled circles in each panel indicate the directions of the protons.

The present results as well as accurate numerical methods will be useful for the understanding of various laser-induced recollision phenomena. Analysis of the high-energy part of the photoelectron spectra of H_2^+ and HeH^{2+} induced by intense laser pulses using the obtained ES DCSs are currently under way.

ACKNOWLEDGMENTS

The authors are grateful to Dr. O. I. Tolstikhin at the Russian Research Center, Kurchatov Institute, for his fruitful discussions. This work was supported by a Grant-in-Aid for scientific research (C) from the Japan Society for the Promotion of Science.

APPENDIX A: COULOMB CORRECTED INDEPENDENT ATOM MODEL

First, we decompose the Schrödinger equation, (1), as

$$H = H^{(1)} + V^{(1)}, \tag{A1}$$
$$= H^{(2)} + V^{(2)}, \tag{A2}$$

with

$$H^{(1)} = -\frac{1}{2}\nabla^2 - \frac{Z_1 + Z_2}{r_1}, \tag{A3}$$
$$V^{(1)} = -\frac{Z_1}{r_1} - \frac{Z_2}{r_2} + \frac{Z_1 + Z_2}{r_1}, \tag{A4}$$
$$H^{(2)} = -\frac{1}{2}\nabla^2 - \frac{Z_1 + Z_2}{r_2}, \tag{A5}$$
$$V^{(2)} = -\frac{Z_1}{r_1} - \frac{Z_2}{r_2} + \frac{Z_1 + Z_2}{r_2}. \tag{A6}$$

Here, $H^{(1)}$ and $H^{(2)}$ are the Hamiltonians for one-center Coulomb systems located at $z = -R/2$ and $R/2$ having the net charge of $Z_1 + Z_2$, respectively, and $V^{(1)}$ and $V^{(2)}$ represent the residual short-range potentials. For the scattering state $|\Psi_{\boldsymbol{k}_i}^{(\pm)}\rangle$, the Lippmann-Schwinger equations corresponding to the above decompositions are

$$|\Psi_{\boldsymbol{k}_i}^{(\pm)}\rangle = |\psi_{\boldsymbol{k}_i,1}^{(\pm)}\rangle + G_1 V^{(1)}|\Psi_{\boldsymbol{k}_i}^{(\pm)}\rangle, \tag{A7}$$
$$|\Psi_{\boldsymbol{k}_i}^{(\pm)}\rangle = |\psi_{\boldsymbol{k}_i,2}^{(\pm)}\rangle + G_2 V^{(2)}|\Psi_{\boldsymbol{k}_i}^{(\pm)}\rangle, \tag{A8}$$

where $G^{(j)}$ and $|\psi_{\boldsymbol{k}_i,j}^{(\pm)}\rangle$ ($j = 1,2$) are the Coulomb Green's functions and scattering solutions for the unperturbed

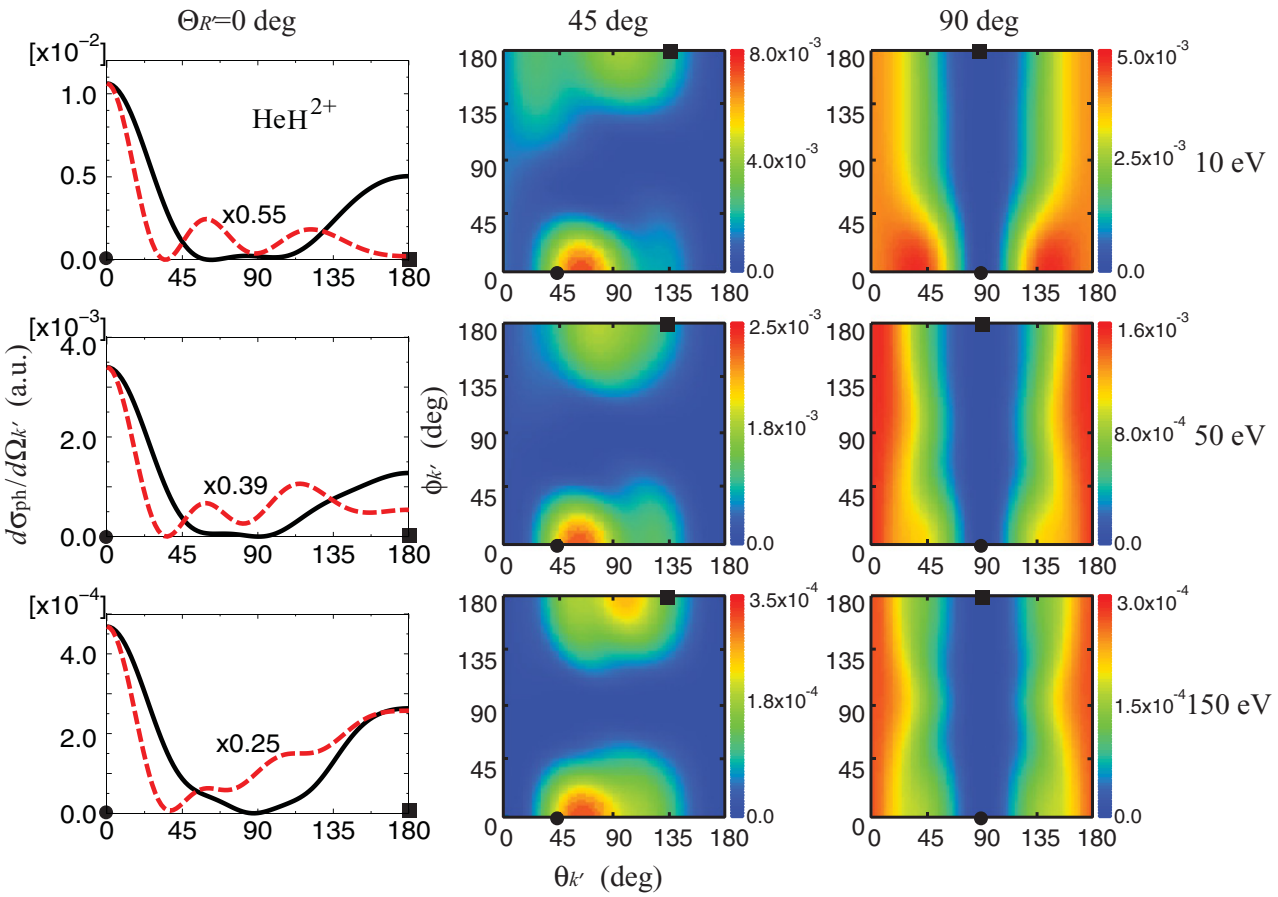

FIG. 4. (Color online) The same as Fig. 3 except PI DCSs of HeH^{2+} ($Z_1 = 2$, $Z_2 = 1$, and $R = 2$) are shown. The filled square in each panel indicates the direction of the charge $Z_1 = 2$ (He^{2+}).

Hamiltonian $H^{(j)}$ ($j = 1,2$), respectively. Multiplying Eq. (A7) by $Z_1/(Z_1+Z_2)$ and Eq. (A8) by $Z_2/(Z_1+Z_2)$, and summing them up, we have the following integral equation:

$$|\Psi^{(\pm)}_{\boldsymbol{k}_i}\rangle = \left[\frac{Z_1}{Z_1+Z_2}|\psi^{(\pm)}_{\boldsymbol{k}_i,1}\rangle + \frac{Z_2}{Z_1+Z_2}|\psi^{(\pm)}_{\boldsymbol{k}_i,2}\rangle\right] + \frac{Z_1 Z_2}{Z_1+Z_2}(G_1-G_2)\left(\frac{1}{r_1}-\frac{1}{r_2}\right)|\Psi^{(\pm)}_{\boldsymbol{k}_i}\rangle. \quad \text{(A9)}$$

Strictly speaking, Eq. (A9) is not a Lippmann-Schwinger equation but is still equivalent to the Schödinger equation (1). Neglecting the second term in Eq. (A9) as a "perturbation," we define the CCIAM wave function by the "distorted-unperturbed" part in the square brackets. The corresponding scattering amplitude, $f_{\rm CCIAM}(\boldsymbol{k},\boldsymbol{k}_i)$, is then defined by the asymptotic form of the CCIAM wave function,

$$\frac{Z_1}{Z_1+Z_2}\psi^{(\pm)}_{\boldsymbol{k}_i,1}(\boldsymbol{r}) + \frac{Z_2}{Z_1+Z_2}\psi^{(\pm)}_{\boldsymbol{k}_i,2}(\boldsymbol{r}) \xrightarrow{r\to\infty} \frac{1}{(2\pi)^{3/2}}\left[e^{i\boldsymbol{k}_i\cdot\boldsymbol{r}+i\gamma\ln[kr(1-\hat{\boldsymbol{k}}_i\cdot\hat{\boldsymbol{r}})]} + f_{\rm CCIAM}(\boldsymbol{k},\boldsymbol{k}_i)\frac{e^{\pm(ikr-i\gamma\ln 2kr)}}{r}\right], \quad \text{(A10)}$$

with

$$f_{\rm CCIAM}(\boldsymbol{k},\boldsymbol{k}_i) = f_1(\boldsymbol{k},\boldsymbol{k}_i) + f_2(\boldsymbol{k},\boldsymbol{k}_i), \quad \text{(A11)}$$

where f_1 and f_2 are the Coulomb scattering amplitudes for the unperturbed Hamiltonians, $H^{(1)}$ and $H^{(2)}$, respectively,

$$f_1(\boldsymbol{k},\boldsymbol{k}_i) = -\frac{\gamma_1 e^{-i\gamma\ln(\sin^2\frac{\theta_k}{2})+2i\sigma_0}}{2k\sin^2\frac{\theta_k}{2}} e^{-i\frac{\boldsymbol{R}\cdot(\boldsymbol{k}-\boldsymbol{k}_i)}{2}}, \quad \text{(A12)}$$

$$f_2(\boldsymbol{k},\boldsymbol{k}_i) = -\frac{\gamma_2 e^{-i\gamma\ln(\sin^2\frac{\theta_k}{2})+2i\sigma_0}}{2k\sin^2\frac{\theta_k}{2}} e^{i\frac{\boldsymbol{R}\cdot(\boldsymbol{k}-\boldsymbol{k}_i)}{2}}. \quad \text{(A13)}$$

Here, $\gamma_1 = -Z_1/k$, $\gamma_2 = -Z_2/k$, and $\boldsymbol{R} = (0,0,R)^t$. Taking the absolute square of Eq. (A11), we have the CCIAM cross section as in Eq. (57).

APPENDIX B: EXPRESSIONS OF THE SPHEROIDAL RADIAL WAVE FUNCTION USING THE *R* MATRIX

The R matrix provides the expression of the spheroidal radial wave function $\Pi^k_{|m|q}(\xi)$. From the recurrence relation [Eq. (53)], the expression at each boundary $\{\bar{\xi}_n\}_{n=1}^{N_{\rm sec}}$ is derived:

$$\Pi^k_{|m|q}(\bar{\xi}_-) = \left(\frac{\bar{\xi}_+^2-1}{\bar{\xi}_-^2-1}\right)^{1/2}\left(1+\frac{\mathcal{R}^{--}_{|m|q}}{\mathscr{R}_{|m|q}(\bar{\xi}_-)}\right)^{-1} \times \frac{\mathcal{R}^{-+}_{|m|q}}{\mathscr{R}_{|m|q}(\bar{\xi}_+)}\Pi^k_{|m|q}(\bar{\xi}_+). \quad \text{(B1)}$$

In each sector other than the first sector, the wave function at each DVR point $\{\xi(x_i)|\xi(x_i) \in [\bar{\xi}_-,\bar{\xi}_+],\ i = 1,\ldots,N_x\}$ is expressed as

$$\Pi^k_{|m|q}[\xi(x_i)] = \left(\frac{\bar{\xi}_+^2 - 1}{\xi^2(x_i) - 1}\right)^{1/2} \left(\frac{\mathcal{R}^{i+}_{|m|q}}{\mathscr{R}_{|m|q}(\bar{\xi}_+)} - \frac{\mathcal{R}^{i-}_{|m|q}\mathcal{R}^{-+}_{|m|q}}{(\mathscr{R}_{|m|q}(\bar{\xi}_-) + \mathcal{R}^{--}_{|m|q})\mathscr{R}_{mq}(\bar{\xi}_+)}\right)\Pi^k_{|m|q}(\bar{\xi}_+), \quad \text{(B2)}$$

where

$$\mathcal{R}^{i\pm}_{|m|q} = [(\xi^2(x_i) - 1)(\bar{\xi}_\pm^2 - 1)]^{1/2} \times \sum_{n=1}^{N_x} \frac{\bar{\Pi}_{|m|q}[\xi(x_i)]\bar{\Pi}_{|m|q}(\bar{\xi}_\pm)}{\bar{E}_n - E}. \quad \text{(B3)}$$

In the first sector, the expression is

$$\Pi^k_{|m|q}[\xi[\mu(x_i)]] = 2\bar{\mu}_+ \left(\frac{\bar{\mu}_+^3 + 2\bar{\mu}_+}{\mu^3(x_i) + 2\mu(x_i)}\right)^{1/2} \times \frac{\tilde{\mathcal{R}}^{i+}_{mq}}{\mathscr{R}_{|m|q}(\bar{\xi}_1)}\Pi^k_{|m|q}(\bar{\xi}_1), \quad \text{(B4)}$$

where

$$\tilde{\mathcal{R}}^{i+}_{mq} = [(\mu^3(x_i) + 2\mu(x_i))(\bar{\mu}_+^3 + 2\bar{\mu}_+)]^{1/2} \times \sum_{n=1}^{N_x} \frac{\tilde{\Pi}_{|m|q}[\xi[\mu(x_i)]]\tilde{\Pi}_{|m|q}[\xi(\bar{\mu}_+)]}{\tilde{E}_n - E}. \quad \text{(B5)}$$

By replacing x_i with $^\forall x \in [-1,1]$ in Eqs. (B2)–(B5), the expression of the wave function at any ξ is obtained. In the calculation of the Gauss-Legendre quadrature integration in Eqs. (27) and (28), we evaluated the values of the spheroidal radial wave function at each DVR quadrature point used in the calculation of the bound state (see Appendix C).

APPENDIX C: NUMERICAL PROCEDURE FOR BOUND STATES

We solve the Schrödinger equation, (1), for the bound state

$$\Psi(\boldsymbol{r}) = \Phi_m(\xi,\eta)\frac{e^{im\phi}}{\sqrt{2\pi}} \quad \text{(C1)}$$

by diagonalizing the two-dimensional Hamiltonian in y and μ in Eqs. (34) and (49), using the direct product of the DVR basis sets associated with Legendre polynomials. Here we present the explicit form of the two-dimensional Schrödinger equation for Φ_m in y and μ:

$$\left\{\frac{2(1-y^2)}{(2-y^2)^{1/2}}\left[\frac{\partial}{\partial\mu}\frac{1}{2}(\mu^3+2\mu)\frac{\partial}{\partial\mu} - \frac{2m^2}{\mu^3+2\mu}\right] + 2\mu\left[\frac{\partial}{\partial y}\frac{1}{2}(1-y^2)(2-y^2)^{1/2}\frac{\partial}{\partial y} - \frac{2m^2}{(1-y^2)(2-y^2)^{1/2}}\right] + 2\mu\frac{2(1-y^2)}{(2-y^2)^{1/2}}\left[a(\mu^2+1) + by(2-y^2)^{1/2} + \frac{R^2}{2}((\mu^2+1)^2 - y^2(2-y^2))E\right]\right\}\Phi_m[\xi(\mu),\eta(y)] = 0. \quad \text{(C2)}$$

Further, we use the scaling for μ as $\mu = \tilde{s}(x+1)$ and diagonalize the generalized eigenvalue problem in x and y. For the ground-state calculation, $N_x = 100$, $N_y = 30$, and $\tilde{s} = \sqrt{40}/2$ are used.

[1] P. B. Corkum, Phys. Rev. Lett. **71**, 1994 (1993).
[2] J. L. Krause, K. J. Schafer, and K. C. Kulander, Phys. Rev. Lett. **68**, 3535 (1992).
[3] T. Morishita, A. T. Le, Z. Chen, and C. D. Lin, Phys. Rev. Lett. **100**, 013903 (2008).
[4] D. Ray, B. Ulrich, I. Bocharova, C. Maharjan, P. Ranitovic, B. Gramkow, M. Magrakvelidze, S. De, I. V. Litvinyuk, A. T. Le, T. Morishita, C. D. Lin, G. G. Paulus, and C. L. Cocke, Phys. Rev. Lett. **100**, 143002 (2008).
[5] M. Okunishi, T. Morishita, G. Prümper, K. Shimada, C. D. Lin, S. Watanabe, and K. Ueda, Phys. Rev. Lett. **100**, 143001 (2008).
[6] S. Minemoto, T. Umegaki, Y. Oguchi, T. Morishita, A.-T. Le, S. Watanabe, and H. Sakai, Phys. Rev. A **78**, 061402 (2008).
[7] O. I. Tolstikhin, T. Morishita, and S. Watanabe, Phys. Rev. A **81**, 033415 (2010).
[8] D. B. Milošević, W. Becker, M. Okunishi, G. Prümper, K. Shimada, and K. Ueda, J. Phys. B **43**, 015401 (2010).
[9] M. V. Frolov, N. L. Manakov, T. S. Sarantseva, and A. F. Starace, Phys. Rev. A **83**, 043416 (2011).
[10] A. Čerkić, E. Hasović, D. B. Milošević, and W. Becker, Phys. Rev. A **79**, 033413 (2009).
[11] M. V. Frolov, N. L. Manakov, and Anthony F. Starace, Phys. Rev. A **79**, 033406 (2009).
[12] J. P. Farrell, L. S. Spector, B. K. McFarland, P. H. Bucksbaum, M. Gühr, M. B. Gaarde, and K. J. Schafer, Phys. Rev. A **83**, 023420 (2011).
[13] H. J. Wörner, H. Niikura, J. B. Bertrand, P. B. Corkum, and D. M. Villeneuve, Phys. Rev. Lett. **102**, 103901 (2009).
[14] J. Higuet, H. Ruf, N. Thiré, R. Cireasa, E. Constant, E. Cormier, D. Descamps, E. Mével, S. Petit, B. Pons, Y. Mairesse, and B. Fabre, Phys. Rev. A **83**, 053401 (2011).
[15] A. D. Shiner, B. E. Schmidt, C. Trallero-Herrero, H. J. Wörner, S. Patchkovskii, P. B. Corkum, J.-C. Kieffer, F. Légaré, and D. M. Villeneuve, Nature Phys. **7**, 464 (2011).
[16] C. D. Lin, A. T. Le, Z. Chen, T. Morishita, and Robert Lucchese, J. Phys. B **43**, 122001 (2010).
[17] M. Okunishi, H. Niikura, R. R. Lucchese, T. Morishita, and K. Ueda, Phys. Rev. Lett. **106**, 063001 (2011).
[18] A. T. Le, R. R. Lucchese, S. Tonzani, T. Morishita, and C. D. Lin, Phys. Rev. A **80**, 013401 (2009).
[19] A. T. Le, R. R. Lucchese, M. T. Lee, and C. D. Lin, Phys. Rev. Lett. **102**, 203001 (2009).

[20] Cheng Jin, Anh-Thu Le, and C. D. Lin, Phys. Rev. A **79**, 053413 (2009).
[21] Anh-Thu Le, R. R. Lucchese, and C. D. Lin, Phys. Rev. A **82**, 023814 (2010).
[22] T. Morishita, T. Umegaki, S. Watanabe, and C. D. Lin, J. Phys. Conf. Ser. **194**, 012011 (2009).
[23] V. L. B. de Jesus, B. Feuerstein, K. Zrost, D. Fischer, A. Rudenko, F. Afaneh, C. D. Schröter, R. Moshammer, and J. Ullrich, J. Phys. B **37**, L161 (2004).
[24] Z. Chen, Y. Liang, and C. D. Lin, Phys. Rev. Lett. **104**, 253201 (2010).
[25] Z. Chen, Y. Liang, and C. D. Lin, Phys. Rev. A **82**, 063417 (2010).
[26] Z. Chen, Y. Liang, D. H. Madison, and C. D. Lin, Phys. Rev. A **84**, 023414 (2011).
[27] H. Niikura, F. Légaré, R. Hasbani, M. Ivanov, D. M. Villeneuve, and P. B. Corkum, Nature (London) **421**, 826 (2003).
[28] S. Baker, J. S. Robinson, C. A. Haworth, H. Teng, R. A. Smith, C. C. Chirilă, M. Lein, J. W. G. Tisch, and J. P. Marangos, Science **312**, 424 (2006).
[29] I. V. Komarov, L. I. Ponomarev, and S. Yu. Slavyanov, *Spheroidal and Coulomb Spheroidal Functions* (Nauka, Moscow, 1976).
[30] D. I. Abramov and I. V. Komarov, Teoret. Mat. Fiz. **22**, 253 (1975) [Theor. Math. Phys. **22**, 179 (1975)].
[31] L. I. Ponomarev and L. N. Somov, J. Comp. Phys. **20**, 183 (1976).
[32] J. Rankin and W. R. Thorson, J. Comp. Phys. **32**, 437 (1979).
[33] G. Hadinger, M. A. Frécon, and G. Hadinger, J. Phys. B **29**, 2951 (1996).
[34] M. Hiyama and H. Nakamura, Comp. Phys. Commun. **103**, 209 (1997).
[35] R. Della Picca, P. D. Fainstein, M. L. Martiarena, and A. Dubois, J. Phys. Conf. Ser. **141**, 012006 (2008).
[36] L. Tao, C. W. McCurdy, and T. N. Rescigno, Phys. Rev. A **79**, 012719 (2009).
[37] X. Guan, E. B. Secor, Klaus Bartschat, and B. I. Schneider, Phys. Rev. A **84**, 033420 (2011).
[38] A. T. Le, R. Della Picca, P. D. Fainstein, D. A. Telnov, M. Lein, and C. D. Lin, J. Phys. B **41**, 081002 (2008).
[39] H. Akagi, T. Otobe, A. Staudte, A. Shiner, F. Turner, R. Dörner, D. M. Villeneuve, and P. B. Corkum, Science **325**, 1364 (2009).
[40] L. Holmegaard, J. L. Hansen, L. Kalhøj, S. L. Kragh, H. Stapelfeldt, F. Filsinger, J. Küpper, G. Meijer, D. Dimitrovski, M. Abu-samha, C. P. J. Martiny, and L. B. Madsen, Nature (London) **6**, 428 (2010).
[41] M. Abu-samha and L. B. Madsen, Phys. Rev. A **82**, 043413 (2010).
[42] H. Ohmura, N. Saito, and T. Morishita, Phys. Rev. A **83**, 063407 (2011).
[43] H. Li, D. Ray, S. De, I. Znakovskaya, W. Cao, G. Laurent, Z. Wang, M. F. Kling, A. T. Le, and C. L. Cocke, Phys. Rev. A **84**, 043429 (2011).
[44] A. Etches, M. B. Gaarde, and L. B. Madsen, Phys. Rev. A **84**, 023418 (2011).
[45] O. I. Tolstikhin, T. Morishita, and L. B. Madsen, Phys. Rev. A **84**, 053423 (2011).
[46] N. F. Mott and H. S. W. Massey, *The Theory of Atomic Collision* (Oxford University Press, New York, 1965).
[47] J. C. Light, I. P. Hamilton, and J. V. Lill, J. Chem. Phys. **82**, 1400 (1985).
[48] O. I. Tolstikhina and H. Nakamura, J. Chem. Phys. **108**, 8899 (1998).
[49] H. Bachau, J. Phys. B **35**, 509 (2002).
[50] B. Pons, Phys. Rev. A **67**, 040702 (2003).
[51] O. I. Tolstikhin, S. Watanabe, and M. Matsuzawa, J. Phys. B **29**, L389 (1996).
[52] P. D. McCaffrey, J. K. Dewhurst, D. W. H. Rankin, R. J. Mawhorter, and S. Sharma, J. Chem. Phys. **128**, 204304 (2008).
[53] J. Xu, Z. Chen, A.-T. Le, and C. D. Lin, Phys. Rev. A **82**, 033403 (2010).